

Supplementary Information: Detection of a Jahn-Teller Mode as an Ultrafast Fingerprint of Spin-transition-induced Charge Transfer in CoFe Prussian Blue Analogue

Marius Hervé,^{*a} Bogdan Marekha,^{b,c,†} Sandra Mazerat,^d Talal Mallah,^d Marco Cammarata,^e Samir F. Matar,^f Stefan Haacke,^b Jérémie Léonard^b and Eric Collet^{*a,g}

^a Univ Rennes, CNRS, IPR (Institut de Physique de Rennes) – UMR 6251, F-35000 Rennes, France.

^b Institut de Physique et Chimie des Matériaux de Strasbourg, Université de Strasbourg, CNRS UMR 7504, Strasbourg, France.

^c Department of Biomolecular Mechanisms, Max Planck Institute for Medical Research, Jahnstr. 29, Heidelberg, 69120, Germany.

^d Université Paris-Saclay, Institut de Chimie Moléculaire et des Matériaux d'Orsay, CNRS, UMR 8182, 91400 Orsay, France.

^e ESRF – The European Synchrotron, 71 avenue des Martyrs, CS40220, 38043 Grenoble Cedex 9, France.

^f Lebanese German University (LGU), Sahel Alma Campus, Jounieh, Lebanon.

^g Institut Universitaire de France (IUF).

[†] Present address: Laboratoire de Chimie de l'ENS de Lyon, French National Centre for Scientific Research (CNRS), 69364, Lyon, France.

Analysis of Transient Absorption Signal

As mentioned in the Main Text, Transient Absorption (TA) spectroscopy data was fitted using three different approaches.

(1) FFT of the residuals of global fit

In a first approach, global fitting of the TA data was performed to extract the main decay dynamics. The fit included a single decay timescale and a constant plateau. Figure S1b shows the Decay-Associated Spectra (DAS) resulting from global fit of TA map with parallel polarizations (Figure S1a, same as Figure 2a of the Main Text). The plateau component (black line) corresponds to the absorption changes in the final HS state, and is similar to the absorption changes displayed in Figure 1c. The obtained residuals of the fit, shown in Figure 2c of the Main Text, display the oscillating part of TA map.

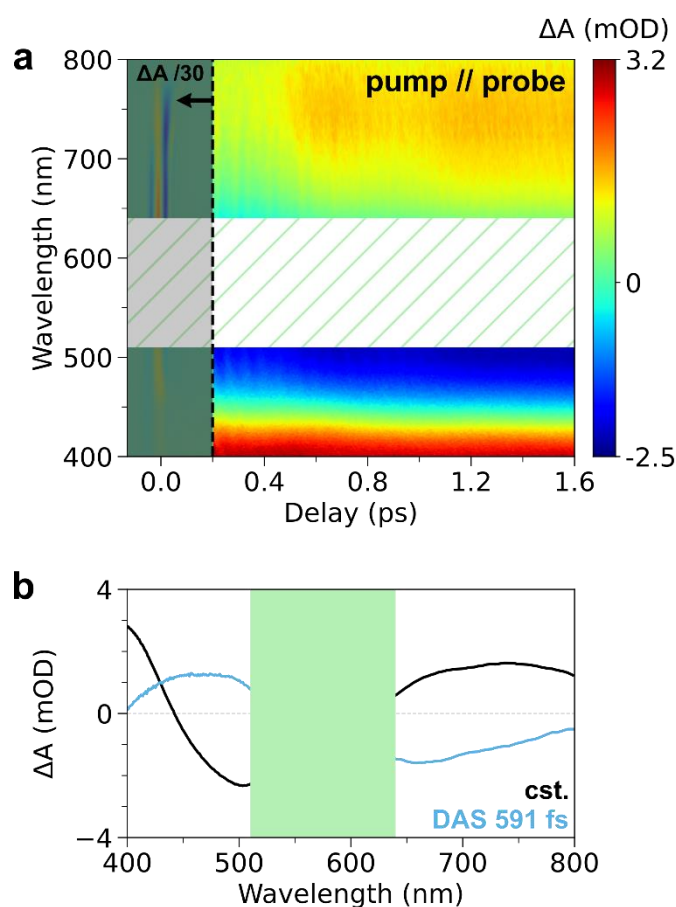


Figure S1. a) TA map of CoFe for parallel pump and probe polarizations (same as Figure 2a of the Main Text). Grey-shaded area corresponds to the CPM contribution at delays below 200 fs, where the intensity is decreased by a factor of 30 to avoid saturation of the colour scale. Green-hatched area corresponds to pump scattering. Both areas are discarded in global fitting. b) Decay-Associated Spectra (DAS) resulting from global fitting of TA map, that represent the intensity of the constant plateau and decay component as a function of probe wavelength. Green-coloured area corresponds to pump scattering.

In order to attribute the oscillatory components observed in the residuals to CoFe nanoparticles, TA measurements were performed on the same cuvette filled with water only (i.e., blank measurement, without any CoFe particle). The associated TA map is shown in Figure S2a,b, for both polarization configurations. It mostly corresponds to Cross-Phase Modulation (CPM) when both pulses overlap at

time delays shorter than 200 fs. FFT of the blank signal after 200 fs is displayed in Figure S2c,d. It shows that oscillations at 515 cm^{-1} are also observed for the blank, over a wide range of wavelength. This corresponds to the response of the cuvette itself, and cannot be attributed to oscillations in the dynamics of CoFe particles. Therefore, it was not considered in the discussion.

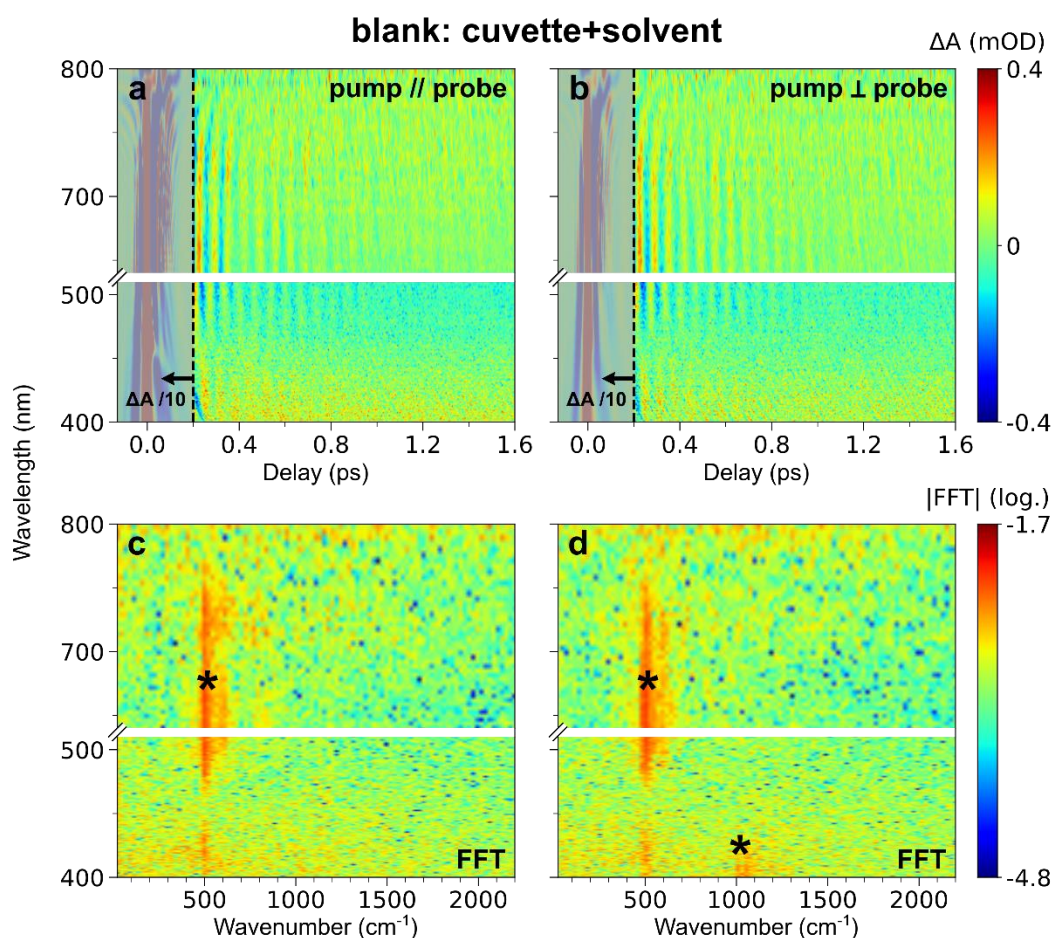


Figure S2. a,b) TA map of the blank (i.e., cuvette+solvent only, no CoFe particle) for parallel (a) and perpendicular (b) pump and probe polarizations. Grey-shaded area corresponds to the CPM contribution at delays below 200 fs. c,d) FFT map of the blank signal after 200 fs (in log scale), for both parallel (c) and perpendicular (d) configurations. Black asterisks (*) correspond to the spurious contributions of the blank, including the oscillation at 515 cm^{-1} reported in Figures 2 and S3. The common colour scale for each row is shown on the right, and is the same as in Figure 2.

Complementary TA measurements were also done on CoFe nanoparticles of a different size (70 nm), at the same concentration¹. Figure S3 shows the same analysis as for 11 nm particles: TA measurements were done in both polarization configurations (Figure S3a,b), fitted by global analysis, and the residuals (Figure S3c,d) were analysed by FFT (Figure S3e,f). The frequencies observed in the FFT map remain the same. In particular, oscillations around 800 cm^{-1} are also visible with an FFT intensity similar to 11 nm particles, and identical TA data are again observed in both parallel and perpendicular polarization configurations. As the 70 nm particles have a core-to-shell ratio that is ~ 6 times greater than the 11 nm particles, any contribution in the TA signal from the passive $\text{Co}^{\text{II}}\text{Fe}^{\text{II}} + \text{Co}^{\text{II}}\text{Fe}^{\text{III}}$ shell or from the PVP polymer covering the particles (Resonant Impulsive-Stimulated Raman Scattering...) should be decreased by a factor of 6 when changing the particle size. As this is not observed in the present measurements, the TA signal solely stems from the photoactive $\text{Co}^{\text{III}}\text{Fe}^{\text{II}}$ pairs present in the core of the particles, whose concentration is barely affected by the size of the particles.

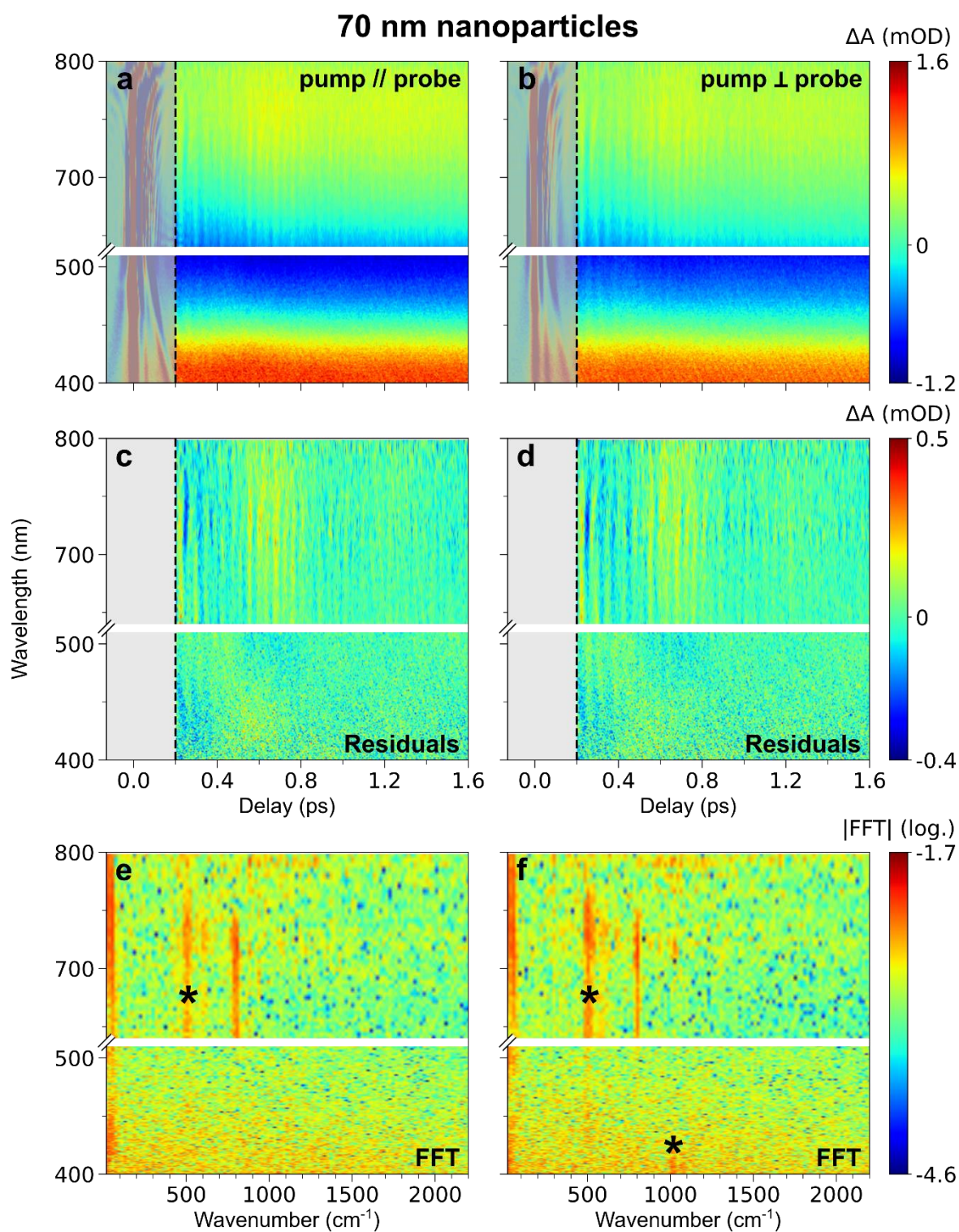


Figure S3. TA data for 70 nm particles, following the same analysis as for 11 nm particles. a,b) TA map for parallel (a) and perpendicular (b) polarization configurations. c,d) residuals of global fitting after 200 fs, in parallel (c) and perpendicular (d) configurations. e,f) FFT map of the residuals (in log scale), for parallel (e) and perpendicular (f) configurations. Black asterisks (*) indicate the spurious oscillations from the blank. For all the maps, the grey-shaded area corresponds to the CPM contribution. The common colour scale for each row is shown on the right.

(2) Single ESA decay kinetics: least-square fit

In a second approach, the TA signal was spectrally integrated over the Excited State Absorption (ESA) band from 650 nm to 740 nm, where oscillations around 800 cm^{-1} are predominant. The corresponding kinetic trace $\Delta A^{\text{ESA}}(t)$ was first fitted using a least-square procedure, with the sum of an exponential decay contribution and a series of three damped oscillations:

$$\begin{aligned} \Delta A_{\text{fit}}(t) &= \Delta A_{\text{exp}}(t) + \sum_{i=1}^3 \Delta A_{\text{osc}}^i(t) \\ &= A_{\text{cst}} + A_{\text{exp}} \cdot \left[1 - \exp\left(-\frac{t}{\tau_{\text{SP}}}\right) \right] + \sum_{i=1}^3 A_i \cdot \exp\left(-\frac{t}{\tau_{\text{damp}}^i}\right) \cdot \cos(\omega_i t + \varphi_i) \end{aligned}$$

Where τ_{SP} is the decay timescale associated to the structural relaxation around the small polarons, and ω_i , τ_{damp}^i and φ_i are the frequency, damping rate and phase of each oscillatory feature. As an example, the result of the fit of $\Delta A^{\text{ESA}}(t)$ in the parallel configuration for 11 nm particles is shown in Figure S4. In this specific configuration, the obtained decay is $\tau_{\text{SP}} = 455 \pm 8$ fs, and the oscillations frequencies are $\omega_1 = 58.4 \pm 0.4$ cm^{-1} , $\omega_2 = 515 \pm 2$ cm^{-1} and $\omega_3 = 798 \pm 2$ cm^{-1} , with damping rates of $\tau_{\text{damp}}^1 = 830 \pm 40$ fs, $\tau_{\text{damp}}^2 = 230 \pm 20$ fs and $\tau_{\text{damp}}^3 = 700 \pm 100$ fs respectively (the uncertainties given here correspond to the standard deviation of the least-square fit in this configuration). Both values of τ_{SP} and ω_1 agree with the previous measurements².

Least-square Fit

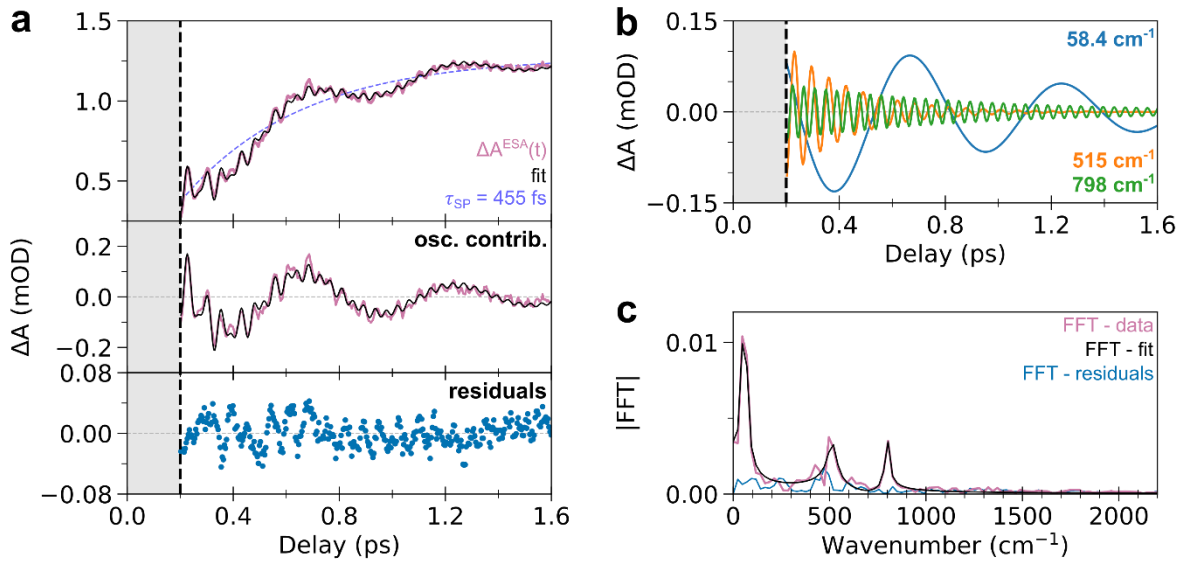


Figure S4. a) Top panel: least-square fit of $\Delta A^{\text{ESA}}(t)$ with $\Delta A_{\text{fit}}(t)$: the integrated transient is shown in magenta, together with the resulting full fit in black and the exponential contribution of the fit, $\Delta A_{\text{exp}}(t)$ (light purple dashed line). Middle panel: oscillatory contribution of $\Delta A^{\text{ESA}}(t)$ (magenta line), obtained by subtracting $\Delta A_{\text{exp}}(t)$ to $\Delta A^{\text{ESA}}(t)$. The oscillatory part of the fit is also shown (black line). Bottom panel: residuals of the fit. b) Individual contributions of each of the three oscillatory features obtained from the fit, $\Delta A_{\text{osc}}^i(t)$ ($i=1-3$). c) FFT of the oscillatory contribution of $\Delta A^{\text{ESA}}(t)$ (magenta line), of the oscillatory part of the fit (black line) and of the residuals (blue line).

(3) Single ESA decay kinetics: LPSVD analysis

We also used Linear Prediction and Singular Value Decomposition (LPSVD)³⁻⁵ to extract the oscillatory components of $\Delta A^{\text{ESA}}(t)$. The result in the parallel configuration for 11 nm particles is shown in Figure S5, and includes 2 non-oscillating components (equivalent to the single exponential and constant offset in the least-square fit above) and 3 oscillation frequencies. In this specific configuration, the obtained frequencies are 61 cm^{-1} , 506 cm^{-1} and 796 cm^{-1} , that are close to the values obtained by least-square fit. Overall, least-square fit and LPSVD analysis give similar results, with nearly identical residuals (Fig S4a and Fig S5a) and regression standard errors (of typically $<2 \cdot 10^{-5}$).

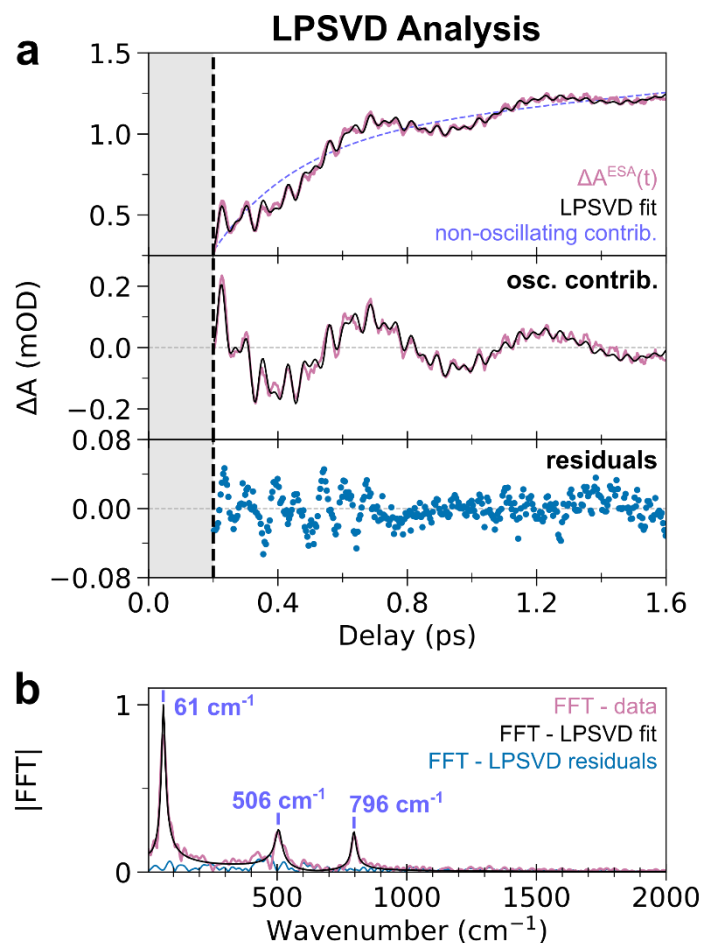


Figure S5. a) Top panel: LPSVD analysis (black) of the spectrally-integrated $\Delta A^{\text{ESA}}(t)$ (magenta), together with the non-oscillating components of the analysis (light purple dashed line). Middle panel: oscillatory contribution of $\Delta A^{\text{ESA}}(t)$ (magenta line), obtained by subtracting the non-oscillating contribution to $\Delta A^{\text{ESA}}(t)$. The oscillatory component of LPSVD is also shown (black line). Bottom panel: residuals of the LPSVD fit. b) FFT of the oscillatory contribution of $\Delta A^{\text{ESA}}(t)$ (magenta line), of the oscillatory component of LPSVD (black line) and of the residuals (blue line).

Table S1 summarizes the values of the decay constants (τ_{SP}), oscillation frequencies (ω_1 , ω_3) and damping rates (τ_{damp}^1 , τ_{damp}^3) extracted from least-square fit and LPSVD analysis, for the different sizes of particles and polarization configurations. For all the parameters, a good agreement is found between least-square fit and LPSVD analysis. In the case of oscillations frequencies and damping rates, the obtained values are not dependent on the particle size, nor on the relative pump and probe polarizations. Thus, the values reported in the Main Text correspond to the average of the values

extracted using both fitting procedures in the four different experimental configurations (8 values in total for each parameter). In the case of τ_{SP} , the obtained values depend on the particle size, and the average value for each particle size is considered. For all the averaged values, the reported error bar corresponds to the standard deviation of the averaged ensemble.

The dependence of τ_{SP} in the particle size can be possibly explained by the nature of the associated relaxation process. As explained in the Main Text, τ_{SP} corresponds to the timescale of the structural reorganizations around the small-polaron (SP) created by the STICT process. Such a structural reorganization results from the relaxation of the strain induced by the new Co-N bond lengths of the $\text{Co}^{\text{II}}\text{Fe}^{\text{III}}$ polaron on the surrounding PBA lattice. It therefore depends on the particle expansion and occurs on a time scale which, given the small size of the present PBA nanocrystals (11 nm and 70 nm), depends on the particle size. In the Main Text, only the value for 11 nm particles is considered for the discussion, but the interpretation of the oscillatory features remains the same for 70 nm particles.

		11 nm		70 nm	
		//	\perp	//	\perp
τ_{SP}	Least-square fit	455 fs	490 fs	250 fs	270 fs
	LPSVD analysis	403 fs	441 fs	188 fs	208 fs
	average	450\pm40 fs		230\pm40 fs	
ω_1	Least-square fit	58.4 cm^{-1}	57.4 cm^{-1}	59.5 cm^{-1}	58.7 cm^{-1}
	LPSVD analysis	61.2 cm^{-1}	59.6 cm^{-1}	63.0 cm^{-1}	60.4 cm^{-1}
	average	60\pm2 cm^{-1}			
ω_3	Least-square fit	798 cm^{-1}	800 cm^{-1}	799 cm^{-1}	800 cm^{-1}
	LPSVD analysis	796 cm^{-1}	799 cm^{-1}	797 cm^{-1}	797 cm^{-1}
	average	798\pm2 cm^{-1}			
τ_{damp}^1	Least-square fit	830 fs	760 fs	700 fs	720 fs
	LPSVD analysis	710 fs	790 fs	470 fs	550 fs
	average	690\pm120 fs			
τ_{damp}^3	Least-square fit	700 fs	820 fs	1030 fs	1190 fs
	LPSVD analysis	820 fs	850 fs	1010 fs	1220 fs
	average	960\pm180 fs			

Table S1. Summary of the fit results in the four different experimental configurations, for both fitting procedures: small-polaron decay τ_{SP} , oscillation frequencies ω_1 and ω_3 , and damping rates τ_{damp}^1 and τ_{damp}^3 . The average value of each parameter is also shown.

For the comparison of $\Delta A^{\text{ESA}}(t)$ between parallel and perpendicular polarization configurations (Figure 3a of the Main Text), we used the fitted phase of the 60 cm^{-1} oscillations as a reference for time 0. Doing so, a corresponding phase difference between parallel and perpendicular configurations of 13 fs was corrected (with a precision of 8 fs, estimated from the standard deviation of the 60 cm^{-1} phase in the least-square fit). It mostly originates from differences in chirp correction between the two TA measurements. Additionally, the least-square fits enable to estimate a precision of 2 fs in the phase of the 798 cm^{-1} oscillations, that ensures a confident analysis of phase relationship between the different

configurations. After this correction, the TA data in both parallel and perpendicular pump-probe polarizations have similar phases and amplitudes over the explored delay range (Figure 2, 3 and S3). The invariance with respect to the polarization configuration can be possibly explained by electronic dephasing before 200 fs⁶, by ensemble averaging over all the possible orientations of the nanocrystals in suspension, by different possible probe transitions, or, in the case of 798 cm⁻¹ oscillations, by the modulation of absorption by Q_{JT}^2 , that is insensitive to π -phase shifts.

DFT Calculations

As explained in the Main Text, DFT calculations were performed on the $(\text{CN})_5\text{Co-N-C-Fe}(\text{CN})_5^{6-}$ monomer unit, being either in LS, $\text{Co}^{\text{III}}(\text{S}=0)\text{Fe}^{\text{II}}(\text{S}=0)$ state, or in HS, $\text{Co}^{\text{II}}(\text{S}=3/2)\text{Fe}^{\text{III}}(\text{S}=1/2)$ state. The geometry of the LS and HS monomer units is shown in Figure S6, and the associated atomic coordinates are given in Table S3 and S4. As can be seen on Figure S6, slight departure from O_h symmetry is observed for the CoN_6 and FeC_6 octahedra, in both monomer geometries. This is due to the geometry optimization performed for these structures: given that a single monomer is considered here, the 3D cubic network of the PBA crystal is not present to maintain local O_h symmetry. Additionally, the negative charge of the considered monomer is not balanced by the neighbour metallic centres and the counter-ions in the PBA (Cs^+ for the present compound), thus imposing supplementary Coulombic repulsion. Nonetheless, such a model geometry was previously shown to give a qualitative understanding of the (photo-)physical properties of PBAs^{2,7}.

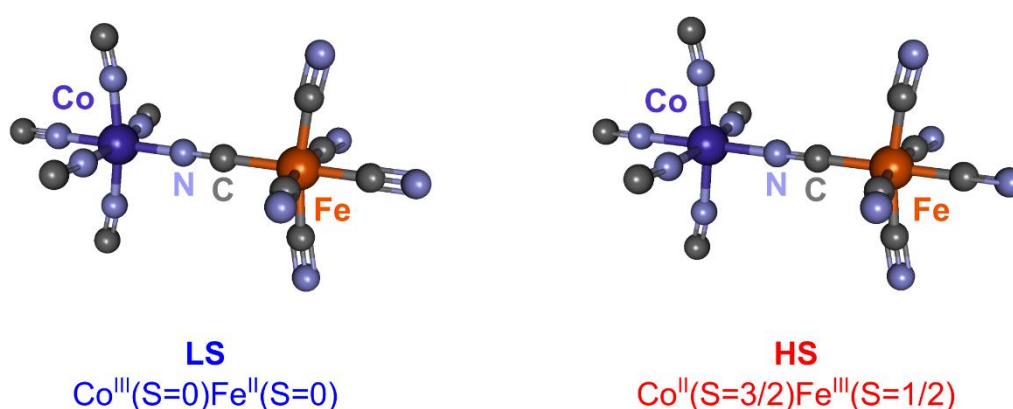


Figure S6. Geometry of the LS and HS monomer units, $(\text{CN})_5\text{Co-N-C-Fe}(\text{CN})_5^{6-}$, used for calculations of vibrational structure. As electronic and spin states differ between the LS and HS states, the Co-N bonds and, to a minor extent, the Fe-C bonds, are lengthened from the LS to the HS geometry.

Vibrational modes were derived for both geometries, and the result is shown in Table S2. In the case of LS monomer, a low-energy negative frequency is observed in calculations (mode No. 1), that is due to difficulties in finding appropriate minimum for this highly negative monomer, and is therefore inherent to the chosen model. The qualitative discussion of higher frequency modes is however not affected. As discussed in the Main Text, both LS and HS states display the typical vibrational structure of PBAs, with global CoN_6 and FeC_6 modes below 530 cm^{-1} , a gap between 530 cm^{-1} and 1980 cm^{-1} , and finally CN stretching modes above 1980 cm^{-1} . This spectral gap is also observed in the infrared spectrum of the CoFe nanoparticles, shown in Figure S7.

No.	Frequency (cm ⁻¹)		No.	Frequency (cm ⁻¹)	
	LS	HS		LS	HS
1	-11.6	9.7	34	340.5	293.0
2	44.6	44.3	35	340.5	299.6
3	44.6	44.3	36	352.5	305.1
4	52.9	46.4	37	357.1	319.6
5	62.7	54.4	38	357.1	319.7
6	62.7	54.4	39	379.1	321.3
7	85.4	80.2	40	384.2	324.0
8	94.8	88.9	41	385.5	324.3
9	94.8	90.3	42	390.6	331.9
10	112.3	90.4	43	390.6	331.9
11	116.0	99.1	44	429.1	364.9
12	116.0	99.1	45	429.1	366.9
13	120.4	104.8	46	440.0	366.9
14	124.7	118.0	47	445.9	430.5
15	133.6	125.0	48	457.4	441.7
16	133.6	125.0	49	457.4	441.7
17	134.4	129.7	50	459.9	460.2
18	145.8	133.1	51	459.9	463.0
19	145.8	133.2	52	468.1	473.7
20	152.1	134.0	53	473.1	473.7
21	211.5	181.1	54	473.2	521.0
22	211.5	189.8	55	473.6	521.0
23	277.8	202.8	56	2042.8	1987.2
24	293.8	202.8	57	2096.2	2099.4
25	299.4	236.5	58	2096.2	2100.2
26	299.4	251.7	59	2101.9	2100.3
27	303.9	251.7	60	2103.6	2100.3
28	309.9	258.8	61	2130.0	2103.6
29	315.3	262.1	62	2133.0	2135.7
30	316.0	262.1	63	2133.0	2136.4
31	323.5	277.5	64	2135.0	2136.4
32	323.6	289.7	65	2139.4	2143.2
33	330.5	289.7	66	2142.6	2153.6

Table S2. Calculated vibrational modes for the LS and HS monomers.

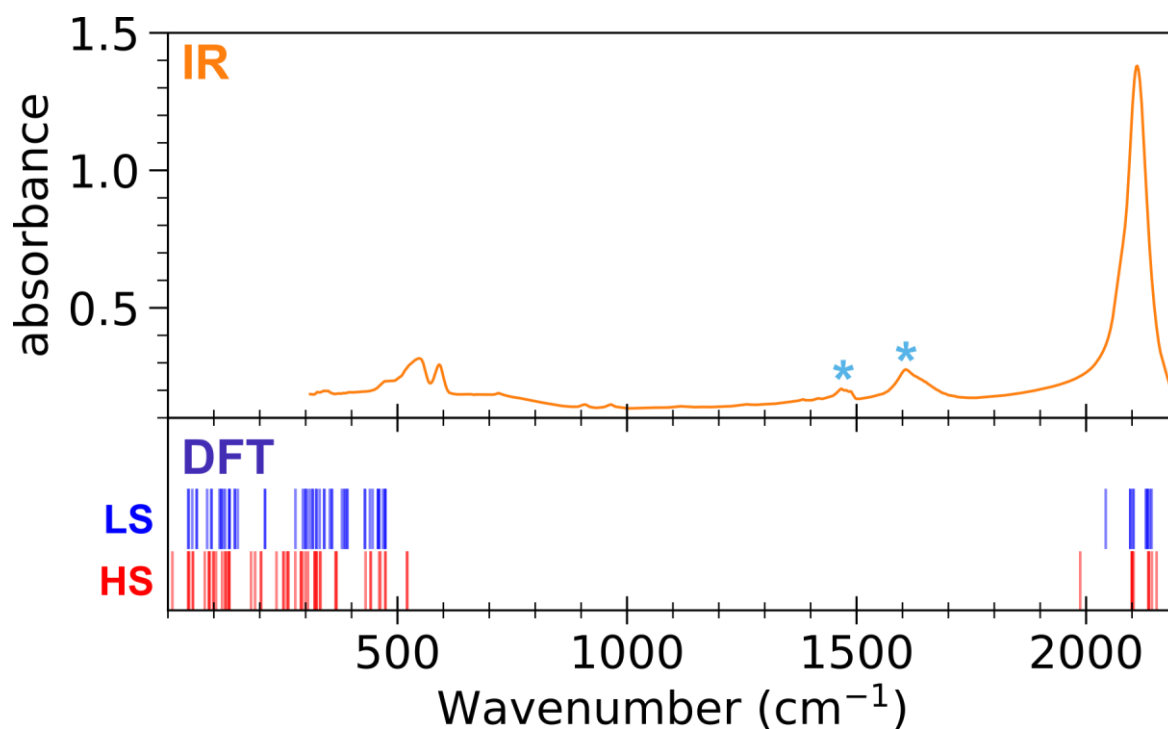
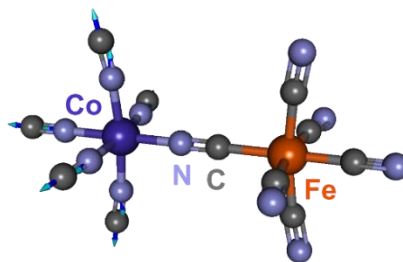


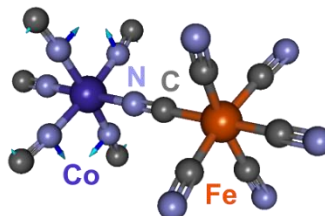
Figure S7. Infrared spectrum of LS CoFe nanoparticles, compared with the vibrational modes obtained from the DFT calculations. Blue asterisks indicate IR absorption from the passive shell of the particles.

Among the ML_6 modes, CoN_6 modes are found around 380 cm^{-1} in LS state, i.e., close to experimentally observed frequency of $\omega_{JT} = 798/2 = 399\text{ cm}^{-1}$. Modes No. 39, 40 and 41 of LS monomer are represented in Figure S7, and can be seen in Supplementary Videos S1-S3. In particular, mode No. 39 is a CoN_6 breathing mode (379.1 cm^{-1}), and mode No. 41 is the Jahn-Teller (JT) “ x^2-y^2 ” mode (385.5 cm^{-1}), that is distorted compared to a “pure” JT mode in O_h symmetry. Such a mode therefore corresponds to the JT mode activated in the experiment.

Mode 39: 379.1 cm⁻¹
CoN₆ "breathing"-like mode



Mode 40: 384.2 cm⁻¹
CoN₆ "pincer"-like mode



Mode 41: 385.5 cm⁻¹
CoN₆ JT "x²-y²"-like mode

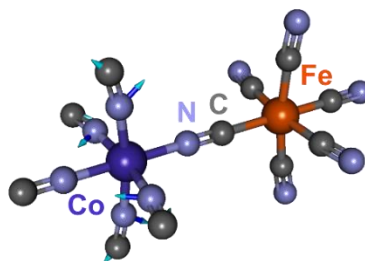


Figure S7. Representation of selected CoN₆ modes for the LS monomer unit: modes No. 39, 40 and 41, whose energies are around 380 cm⁻¹. For each mode, the blue arrows represent the atomic displacements associated to the normal mode.

Model of the Temporal Evolution along the Breathing and Jahn-Teller Modes

As discussed in the Main Text, the STICT process involves the activation of both CoN₆ breathing and Jahn-Teller modes on the ultrafast timescale. In the TA data, this gives rise to oscillatory signatures assigned to coherent oscillations in the final state (i.e., after the STICT process), attributed to the Jahn-Teller mode but not to the breathing mode. To explain the observation of coherent signatures for the Jahn-Teller mode only, we propose the model below for the time evolution along these two modes during the STICT process.

Previous work on CoFe² has established that light absorption generates initial population in the photo-excited (PE) state, that subsequently undergoes the spin transition within $\tau_{ST} = 50$ fs towards a mediator (MED) state, followed by charge transfer within $\tau_{CT} = 200$ fs. This process leads to the creation of a small-polaron (SP), that undergoes structural reorganizations in $\tau_{SP} = 450$ fs, ending in the final HS state. In the following, we consider how the whole STICT process affects the vibrational dynamics along the two modes Q_B and Q_{JT} . As schematically shown in Figure 4 of the Main Text, the initial PE state is displacive along both Q_B and Q_{JT} modes. In the rest of the process, dynamics are affected differently along these two modes. We thus separate the temporal evolution of each mode by considering its evolution firstly in the PE state, starting from the initial LS geometry, and secondly after the PE state, towards the final HS state:

$$Q_B(t) = Q_B^{LS} + \Delta Q_B^{PE}(t) + \Delta Q_B^{HS}(t)$$

$$Q_{JT}(t) = Q_{JT}^{LS} + \Delta Q_{JT}^{PE}(t) + \Delta Q_{JT}^{HS}(t)$$

We describe thereafter the general evolution in the PE state and after this state, for any of the two modes, before stating the differences between Q_B and Q_{JT} in these dynamics.

(1) Temporal evolution in the PE state

Given that the PE state is displacive along both coordinates, impulsive photoexcitation – i.e., with a pump pulse duration shorter than each mode frequency - in the Franck-Condon zone triggers vibrational coherences along both modes. Such coherences, for a generic vibrational mode Q , can be classically described as damped oscillations, around the new equilibrium position in the PE state:

$$\Delta Q^{PE}(t) = \left[\Delta Q^{PE} + A^{PE}(t) \cdot \exp\left(-\frac{t}{\tau_{damp}}\right) \cdot \cos(\omega \cdot t + \varphi^{PE}) \right] \cdot P^{PE}(t)$$

Where $\Delta Q^{PE} = Q^{PE} - Q^{LS}$, $\omega = 2\pi/T$ is the frequency of the mode Q , with a damping rate of τ_{damp} , an amplitude $A^{PE}(t)$ and an initial phase of φ^{PE} . $\Delta Q_B^{PE}(t)$ is weighted by the population in the PE state, $P^{PE}(t)$, as it decays with time towards the MED state ($P^{PE}(t) = \exp(-t/\tau_{ST})$). We also considered a time-dependent amplitude of the damped oscillations, expressed as:

$$A^{PE}(t) = A^{PE} \cdot \left[1 - \exp\left(-\frac{t}{\tau_{disp}}\right) \right] + \Delta Q^{PE} \cdot \exp\left(-\frac{t}{\tau_{disp}}\right)$$

Such a time dependence is chosen to model the displacive character of the PE state: at $t=0$, it imposes a strong driving force for the wavepacket ($A^{PE}(t=0) = \Delta Q^{PE}$), that is reduced at long delays to A^{PE} ($< \Delta Q^{PE}$). We chose $\tau_{disp} = T/4$ for each mode, as it represents the time needed for a wavepacket to move from the initial position (Q^{LS}) to the bottom of the potential energy curve (Q^{PE}), i.e., to reach the new equilibrium position.

(2) Temporal evolution from PE to HS

Along both modes, the evolution from PE to HS is also displacive as the two states have different equilibrium position (see Figure 4a,b of the Main Text). Vibrational coherences along these modes could therefore be triggered in the final HS state as well. However, contrary to the dynamics in the PE state, such coherent oscillations are not instantaneously triggered, but are seeded by the ultrafast processes transferring the population from PE to HS. We thus describe this seeded motion, again for a generic mode Q , as:

$$\Delta Q^{HS}(t) = P_{PE \rightarrow HS}(t) \otimes \delta q^{HS}(t)$$

Where $\delta q^{HS}(t')$ corresponds to damped oscillations in the HS state if they were instantaneously triggered:

$$\delta q^{HS}(t') = \Delta Q^{HS} + A^{HS} \cdot \exp\left(-\frac{t'}{\tau_{damp}}\right) \cdot \cos(\omega t' + \varphi^{HS})$$

With $\Delta Q^{HS} = Q^{HS} - Q^{LS}$.

$P_{PE \rightarrow HS}(t)$ corresponds to the population transfer that seeds the oscillations, i.e., the process that is mainly responsible for the change of equilibrium position along each mode (ST, CT or SP relaxation).

(3) Overall temporal evolution along both modes: $Q_B(t)$ and $Q_{JT}(t)$

The overall temporal evolution along each specific mode was then considered. In the PE state, the dynamics along both modes are very similar, as they consist in impulsive damped oscillations around their respective, new, equilibrium position. From PE and HS, dynamics differ along the two modes, as the seeding processes are different, leading to coherence or decoherence.

Along Q_B , the two-step increase of Co-N bond lengths is responsible for the temporal evolution. For the sake of simplicity, we consider in the present model that the first step of increase corresponds to the impulsive dynamics in PE (i.e., $\Delta Q_B^{PE}(t)$), and that $\Delta Q_B^{HS}(t)$ is influenced only by the second step of increase in Co-N bond lengths, that is the structural relaxation around the SP. We therefore consider that oscillations along Q_B in the final HS state are seeded by the second-step SP relaxation (thus within 450 fs), i.e., that $P_{PE \rightarrow HS}(t)$ can be described as:

$$P_{PE \rightarrow HS}^B(t) = \frac{\tau_{SP}}{\tau_{SP} - \tau_{ST}} \cdot \left[\exp\left(-\frac{t}{\tau_{SP}}\right) - \exp\left(-\frac{t}{\tau_{ST}}\right) \right]$$

For the mode period, we used $T_B = 88$ fs from DFT calculations (mode No. 39 in Figure S7). As $T_B < \tau_{SP}$, oscillations in the HS state are strongly dephased by the slow SP relaxation seeding the motion along Q_B . Therefore, the temporal evolution $Q_B(t)$ shows that no oscillations persist in the final state along Q_B (Figure 4c).

On the contrary, changes along Q_{JT} after the PE state occur only during the transfer from PE to MED, as $Q_{JT}^{ES} \neq 0$ but $Q_{JT}^{MED} = Q_{JT}^{HS} = 0$. Therefore, we considered that the oscillations along Q_{JT} in the final state are seeded by the PE-to-MED ST only (thus within 50 fs), i.e., that $P_{PE \rightarrow HS}(t)$ can be described as:

$$P_{PE \rightarrow HS}^{JT}(t) = \exp\left(-\frac{t}{\tau_{ST}}\right)$$

For the mode period, we used the value extracted from the TA experiments, $T_{JT} = 84$ fs ($\omega_{JT} = 399 \text{ cm}^{-1}$). Given that $T_{JT} > \tau_{ST}$, oscillations along Q_{JT} are visible in the final state (Figure 4d),

giving rise to the coherent signature observed in the experiment. Therefore, while being not complete, this model reasonably accounts for the experimental fingerprints of Jahn-Teller activation. While the two modes have close periods, the model qualitatively shows that the attribution of the coherent oscillations to the Jahn-Teller mode and not to the breathing mode is due to a different activation process for both modes: Following the initial dynamics in the PE state, Q_B is slowly activated by the SP relaxation, while Q_{JT} is rapidly activated by the ST.

(4) Additional parameters for the model

The following, additional, parameters were used to compute Figure 4c and 4d:

- $\tau_{damp}^B = 300$ fs;
- $\Delta Q_B^{PE} = \Delta Q_B^{HS} / 2$ (assuming that Q_B^{PE} is at halfway between Q_B^{HS} and Q_B^{LS});
- $\varphi_B^{PE} = \varphi_B^{HS} = \pi$ (as $Q_B^{LS} < Q_B^{PE} < Q_B^{HS}$);
- $\tau_{damp}^{JT} = 960$ fs (from the TA data);
- $\varphi_{JT}^{PE} = \pi$ (as $Q_{JT}^{LS} < Q_{JT}^{PE}$);
- $\varphi_{JT}^{HS} = 0$ (as $Q_{JT}^{PE} > Q_{JT}^{HS}$).

Detection of a Jahn-Teller Mode in TA Experiments

As explained in the Main Text, JT modes belong to the E_g representation in O_h symmetry. As a consequence, their activation results in the modulation of the absorption properties following Q_{JT}^2 , as the linear optical properties belong to the A_{1g} representation and $A_{1g} \subset E_g \times E_g$. This can also be seen from the geometry of the JT modes. Figure S8 illustrates the temporal evolution of the CoN_6 octahedron in the specific case of the activation of the x^2-y^2 JT mode, that can be described in a classical picture as:

$$Q_{JT}(t) = Q_0 \begin{vmatrix} \sin(\omega_{JT}t) & \\ -\sin(\omega_{JT}t) & \\ 0 & 0 \end{vmatrix} = \begin{vmatrix} Q_x \\ Q_y \\ 0 \end{vmatrix}$$

Where Q_x (Q_y) is the difference in distance between N_x (N_y) atoms, $Q_x = -Q_y$. When activated, this mode first elongates the Co-N bonds along the x axis (increase of Q_x , first panel in Figure S8), while shortening the Co-N bonds along the y axis (decrease of Q_y). Half a period after, the situation is reversed, with the Co- N_x bonds shortened and the Co- N_y bonds elongated, but this geometry is equivalent to the initial one by a rotation of 90° around the z axis. The influence of $Q_{JT}(t)$ on the absorption properties can be described by expanding the optical transition dipole moment along Q_{JT} :

$$d_{fi} = |\langle \psi_f | \vec{d} | \psi_i \rangle| = d_{fi}^0 + \Delta d_{fi,x}^{(1)} \cdot Q_x + \Delta d_{fi,y}^{(1)} \cdot Q_y + \frac{1}{2} \Delta d_{fi,x}^{(2)} \cdot Q_x^2 + \frac{1}{2} \Delta d_{fi,y}^{(2)} \cdot Q_y^2$$

And thus its influence on the absorption changes is:

$$\Delta OD \propto \Delta d_{fi}^2 = \left| \Delta d_{fi}^{(1)} + \Delta d_{fi}^{(2)} \right|^2$$

With

$$\Delta d_{fi}^{(1)} = \Delta d_{fi,x}^{(1)} \cdot Q_x + \Delta d_{fi,y}^{(1)} \cdot Q_y$$

$$\Delta d_{fi}^{(2)} = \frac{1}{2} \Delta d_{fi,x}^{(2)} \cdot Q_x^2 + \frac{1}{2} \Delta d_{fi,y}^{(2)} \cdot Q_y^2$$

Given the O_h symmetry for CoN_6 core, we have $\Delta d_{fi,x}^{(1)} = \Delta d_{fi,y}^{(1)}$, and therefore the first-order term $\Delta d_{fi}^{(1)}$ vanishes as $Q_x = -Q_y$. Consequently, only second-order terms $\Delta d_{fi}^{(2)}$ contribute to ΔOD , as shown on the second panel of Figure S8. This corresponds to a modulation following Q_{JT}^2 , i.e., a modulation of OD at $2\omega_{JT}$, where absorption properties are the same every half Jahn-Teller period because of the equivalence in geometry.

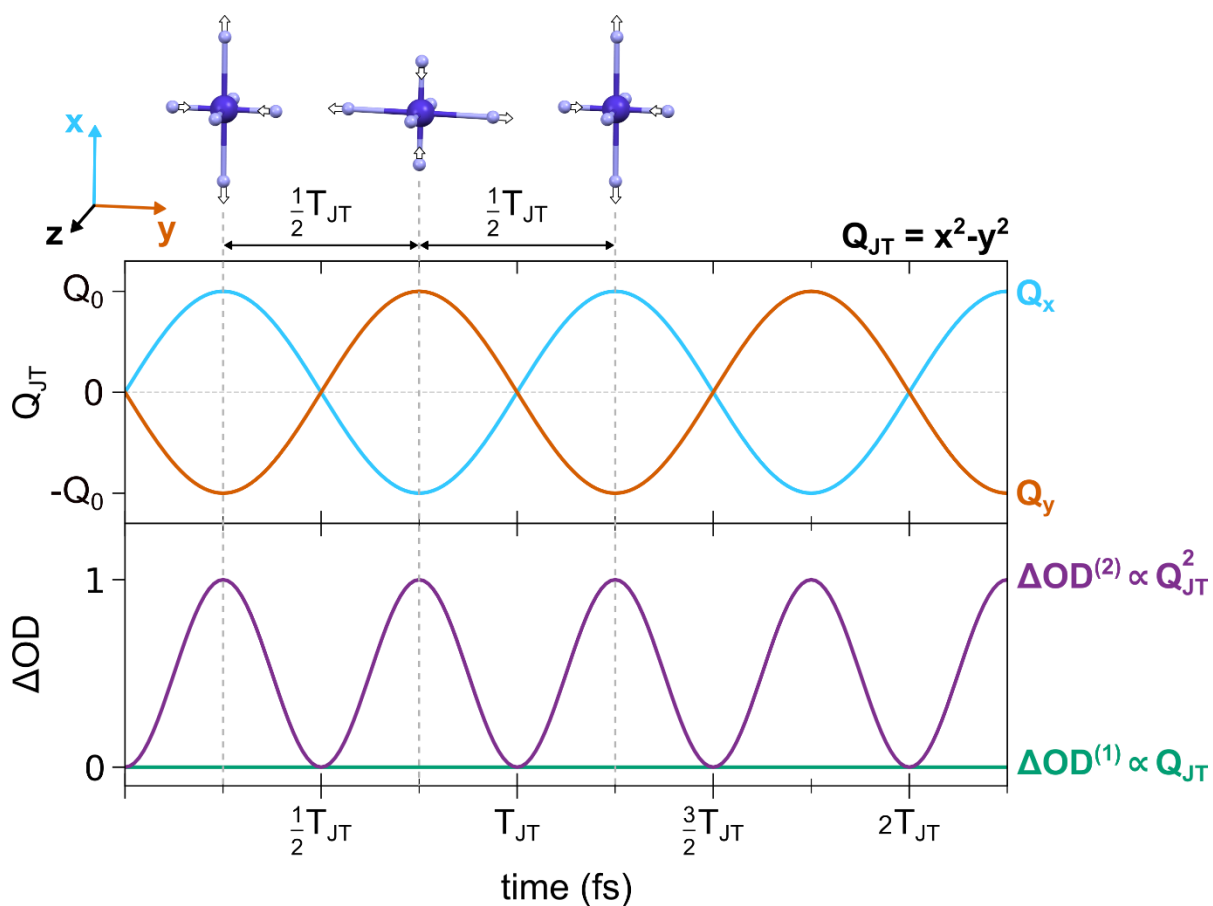


Figure S8. Schematic representation of the temporal modulation of absorption properties with Q_{JT} , in the case of an optical excitation that activates the x^2-y^2 JT mode. First panel: temporal evolution of the two components of Q_{JT} along x (blue curve) and y (orange curve). Second panel: decomposition of ΔOD into the linear and quadratic Q_{JT} dependence, $\Delta OD^{(1)}$ (green curve) and $\Delta OD^{(2)}$ (purple curve), that respectively depend on $\Delta d_{fi}^{(1)}$ and $\Delta d_{fi}^{(2)}$. An illustration of the temporal evolution of the JT mode is shown above the panels.

DFT Structures

C	0.5353790000	-0.0000020000	-0.0000090000
N	-0.6577930000	-0.0001640000	-0.0000420000
C	2.8410900000	-1.3355480000	-1.4264000000
N	3.0602570000	-2.1321530000	-2.2762530000
C	2.8413510000	-1.4263690000	1.3353780000
N	3.0606300000	-2.2767340000	2.1314030000
C	4.6090270000	0.0000450000	-0.0004340000
N	5.7939540000	0.0001160000	-0.0006060000
C	2.8413750000	1.3351710000	1.4264800000
N	3.0606650000	2.1312630000	2.2767810000
C	2.8410550000	1.4266220000	-1.3353090000
N	3.0601940000	2.2775680000	-2.1307550000
N	-4.5893720000	-0.0000180000	0.0000630000
N	-2.8032280000	1.2666830000	1.4171620000
N	-2.8032960000	1.4170890000	-1.2667350000
N	-2.8033600000	-1.2663430000	-1.4174920000
N	-2.8032910000	-1.4175630000	1.2662930000
Fe	2.6709710000	-0.0000030000	-0.0001190000
Co	-2.6522380000	-0.0000560000	0.0000490000
C	-5.7714200000	-0.0000310000	0.0000810000
C	-3.0538280000	-2.0371490000	-2.2784030000
C	-3.0537870000	2.2785790000	-2.0368860000
C	-3.0536720000	-2.2779800000	2.0376780000
C	-3.0536320000	2.0372210000	2.2783300000

Table S3. Atomic coordinates for the geometry of the LS Co^{III}(S=0)Fe^{II}(S=0) monomer unit.

C	-0.6371270000	-0.0064830000	-0.0067340000
N	0.5588530000	-0.0099930000	-0.0086450000
C	-2.9114590000	-1.5695350000	-1.1616950000
N	-3.1516790000	-2.4988100000	-1.8495310000
C	-2.9058050000	1.1601770000	-1.5691040000
N	-3.1426320000	1.8492390000	-2.4983410000
C	-4.6666800000	0.0032580000	0.0040770000
N	-5.8479870000	0.0061040000	0.0072030000
C	-2.8975880000	1.5684630000	1.1593010000
N	-3.1295230000	2.4995290000	1.8475570000
C	-2.9035270000	-1.1608540000	1.5688790000
N	-3.1390110000	-1.8478970000	2.499510000
N	4.8417030000	0.0075670000	0.0064960000
N	2.8481890000	1.7148500000	1.2080180000
N	2.8587090000	-1.2093900000	1.7148960000
N	2.8709550000	-1.7165530000	-1.2088060000
N	2.8613650000	1.2075370000	-1.7164310000
Fe	-2.7260000000	-0.0014450000	-0.0010440000
Co	2.6822710000	-0.0013440000	-0.0012710000
C	6.0282990000	0.0124920000	0.0107380000
C	3.1346010000	-2.6620010000	-1.8759160000
C	3.1156500000	-1.8756380000	2.6627940000
C	3.1196840000	1.8772520000	-2.6615060000
C	3.0993030000	2.6626300000	1.8766490000

Table S4. Atomic coordinates for the geometry of the HS Co^{II}(S=3/2)Fe^{III}(S=1/2) monomer unit.

References

- 1 S. Zerdane, M. Hervé, S. Mazerat, L. Catala, R. Alonso-Mori, J. M. Glownia, S. Song, M. Levantino, T. Mallah, M. Cammarata and E. Collet, *Faraday Discuss.*, 2022, **237**, 224–236.
- 2 M. Cammarata, S. Zerdane, L. Balducci, G. Azzolina, S. Mazerat, C. Exertier, M. Trabuco, M. Levantino, R. Alonso-Mori, J. M. Glownia, S. Song, L. Catala, T. Mallah, S. F. Matar and E. Collet, *Nat. Chem.*, 2021, **13**, 10–14.
- 3 H. Barkhuijsen, R. De Beer, W. M. M. J. Bovée and D. Van Ormondt, *Journal of Magnetic Resonance (1969)*, 1985, **61**, 465–481.
- 4 H. Barkhuijsen, R. De Beer and D. Van Ormondt, *Journal of Magnetic Resonance (1969)*, 1986, **67**, 371–375.
- 5 H. Barkhuijsen, R. De Beer and D. Van Ormondt, *Journal of Magnetic Resonance (1969)*, 1987, **73**, 553–557.
- 6 D. A. Farrow, W. Qian, E. R. Smith, A. A. Ferro and D. M. Jonas, *The Journal of Chemical Physics*, 2008, **128**, 144510.
- 7 J. O. Johansson, J.-W. Kim, E. Allwright, D. M. Rogers, N. Robertson and J.-Y. Bigot, *Chem. Sci.*, 2016, **7**, 7061–7067.